


## Prediction of two-dimensional $\text{Cu}_2\text{C}$ with polyacetylene-like motifs and Dirac nodal line

Busheng Wang<sup>\*</sup> and Gilles Frapper<sup>†</sup>

Applied Quantum Chemistry group, E4 team, IC2MP UMR 7285, Université de Poitiers-CNRS,  
4, rue Michel Brunet, TSA 51106, 86073 Poitiers Cedex 9, France

 (Received 21 December 2020; revised 7 February 2021; accepted 16 February 2021; published 12 March 2021)

The design of novel two-dimensional (2D) materials with unique atomistic configurations and exotic properties are highly desirable for material science. Here, we report the prediction of 2D  $\text{Cu}_2\text{C}$  layers featuring unique carbon motifs with Dirac nodal lines through evolutionary algorithm searches in conjunction with first-principles calculations. The global minimum  $\alpha$ - $\text{Cu}_2\text{C}$  is an exciting new structure featuring one-dimensional (1D) zigzag carbon chains sandwiched by two hexagonal-close-packed copper monolayers, conferring to our predicted ground-state 2D  $\alpha$ - $\text{Cu}_2\text{C}$  an inverse coordination structure. This polyacetylene-like motif (poly- $\text{C}_2$ ) is also encountered in  $\gamma$ - $\text{Cu}_2\text{C}$ . Remarkably, the electronic band structure of  $\alpha$  and  $\gamma$ - $\text{Cu}_2\text{C}$  phases containing polyacetylene-like chains display a 1D Dirac nodal line, which is protected by the glide plane symmetry. Fermi velocities ( $v_f$ ) as high as  $2.45 \times 10^5$  and  $3.85 \times 10^5$  m/s are calculated for  $\alpha$  and  $\gamma$ - $\text{Cu}_2\text{C}$  phases, respectively. This work is an effective effort to design and stabilize the 2D copper carbide layers with exotic structures and nodal lines.

DOI: [10.1103/PhysRevMaterials.5.034003](https://doi.org/10.1103/PhysRevMaterials.5.034003)

### I. INTRODUCTION

Since the discovery of graphene [1–5], two-dimensional (2D) materials have attracted tremendous research interest and have evolved into a vast family of new exciting materials. This diverse group of 2D materials includes boron nitride [6]; graphitic carbon nitride [7,8]; black phosphorus [9,10]; silicene [11,12]; transition metal dichalcogenides [13,14]; transition metal carbides, nitrides, and carbonitrides [15–17]; 2D metals [18,19]; and 2D perovskites [20,21]. The design of such novel 2D materials with unique atomistic configurations and exotic properties is always highly desirable for material science innovation and potential technology application.

Recently, a few theoretical and experimental works have explored the copper-based 2D materials [22–29].  $\text{Cu}_2\text{Si}$  was predicted as a sixfold symmetric 2D material where each Si atom is coordinated to six Cu atoms to form a planar hexacoordinate silicon structure [22]. Then this  $\text{Cu}_2\text{Si}$  monolayer was experimentally synthesized and known to possess two Dirac nodal rings around the  $\Gamma$  point [23]. Meanwhile, the  $\text{Cu}_2\text{Ge}$  monolayer [25] was reported to be isostructural with  $\text{Cu}_2\text{Si}$ . More recent theoretical work reports semiconductor 2D  $\text{CuC}$  monolayers containing planar pentacoordinate carbon (ppC), where  $\text{C}_2$  dimers are embedded into Cu six-membered rings [27]. Based on the above, it is worth asking whether stable 2D  $\text{Cu}_2\text{C}$  materials can be obtained with unique carbon motifs. Furthermore, close-packed 2D copper patches with areas up to  $8 \text{ nm}^2$  were reported as prominent candidates in a graphene template [30], which reveals substantial charge transfer and strong interaction between copper and carbon. This suggested to us that these two elements

together might form interesting 2D  $\text{Cu}_2\text{C}$  with unique geometric topology and exotic electronic properties.

In this work, we investigate overlooked 2D  $\text{Cu}_2\text{C}$  layers by using an evolutionary algorithm, USPEX, in conjunction with first-principles density functional theory (DFT) calculation. The three most stable 2D  $\text{Cu}_2\text{C}$  layers are presented, which contain interesting carbon motifs (1D zigzag carbon chains or  $\text{C}_2$  dimers). Calculations of phonon dispersions and *ab initio* molecular dynamics (AIMD) simulations have confirmed their stability. The global minimum  $\alpha$ - $\text{Cu}_2\text{C}$  is an exciting new 2D structure and has been identified to be partly an ionic compound consisting of 1D zigzag carbon chains and two hexagonal-close-packed copper monolayers playing the roles of anions and cations. Moreover,  $\beta$ - $\text{Cu}_2\text{C}$  is a ppC-containing monolayer, where each C atom binds with four Cu atoms and one neighboring C atom forming a  $\text{C}_2@Cu_6$  subunit in the same plane. Furthermore,  $\gamma$ - $\text{Cu}_2\text{C}$  is a planar-tetracoordinate-carbon-containing monolayer, which also has the 1D zigzag carbon chains, connecting each two hexagonal planar copper ribbons. Most importantly, the  $\alpha$ - and  $\gamma$ - $\text{Cu}_2\text{C}$  layers display a 1D Dirac nodal line in the Brillouin zone, which is protected by the glide plane symmetry. Fermi velocities ( $v_f$ ) as high as  $2.45 \times 10^5$  and  $3.85 \times 10^5$  m/s are calculated for  $\alpha$  and  $\gamma$ - $\text{Cu}_2\text{C}$  phases, respectively. The present work reports on 1D Dirac nodal line materials with high Fermi velocity among a copper-based 2D material family. This work is an effective effort to design and stabilize the 2D copper carbide layers with novel structures and exotic Dirac nodal lines.

### II. COMPUTATIONAL DETAILS

The crystal structure prediction (CSP) searches of 2D  $\text{Cu}_2\text{C}$  structures were performed using an evolutionary algorithm (EA) implemented in the USPEX code [31–35] combined with DFT calculations implemented in the Vienna *ab initio*

\*busheng.wang@univ-poitiers.fr

†gilles.frapper@univ-poitiers.fr

simulation package (VASP version 5.4.4) [36,37]. To perform the fixed-composition EA searches of 2D crystals, several parameters were set up: the thickness of a 2D crystal was restricted in the range of 0 to 4 Å; in each cell, a vacuum region of 15 Å was tested to be sufficient to avoid interactions between the adjacent 2D layers; the randomly 2D structures were within a set of 80 layer space groups (symmetry constraints); primitive unit cells of 3, 6, 12, and 18 atoms were considered ( $Z = 1, 2, 4,$  and  $6,$  respectively). Evolutionary variation operators were applied to produce new structures: 50% of the new structures were produced by heredity, while the remaining structures were produced by atomic mutation (10%), lattice mutations (10%), permutation (10%), and random generation (20%).

First-principles calculations were performed using the projected-augmented-wave method [38] as implemented in VASP. The exchange-correlation energy was treated using the Perdew-Burke-Ernzerhof (PBE) functional [39] at the generalized gradient approximation. Meanwhile, the Heyd-Scuseria-Ernzerhof (HSE06) [40,41] hybrid functional level of theory was also used to properly describe the energy gap, with the optimized PBE structure (single-point energy calculation). This level of theory is noted hereafter as HSE06/PBE. A kinetic cutoff energy of 520 eV was used for the expansion of the wave function and Monkhorst-Pack  $k$  meshes with a grid spacing of  $2\pi \times 0.03 \text{ \AA}^{-1}$  to ensure that the enthalpy converges to better than 1 meV/atom (lower than a chemical accuracy of 1 kcal/mol, i.e., 0.04 eV/atom) [42], and the net force on atoms is below  $1 \times 10^{-3} \text{ eV/\AA}$ . The calculation of the phonon spectra was performed using the density functional perturbation theory [43–45] with VASP and PHONOPY codes [46,47]. Moreover, AIMD simulations in the  $NVT$  ensemble were carried out for 10 ps with a time step of 1.0 fs to evaluate the thermal stability. The temperature was controlled by using the Nosé-Hoover method [48]. Magnetic ground states were checked by spin-polarized calculations with the Hubbard  $U$  correction [49].

To perform chemical-bonding analysis, we carry out density of states (DOS), the solid state adaptive natural density partitioning (SSAdNDP) calculations [50], the crystal overlap Hamilton population (COHP, using the LOBSTER package [51]), and the electron localization function [52] (ELF) from the optimized geometries obtained from PBE calculations. For SSAdNDP calculations, standard Gaussian-type atom-centered basis sets were used for the projection and were trimmed of any functions with angular momentum  $l \geq 4$  as well as diffuse functions with exponents  $< 0.1$ . These basis sets were selected so that on average less than 1% of the density of each occupied plane wave band was lost in projecting into the atomic orbital basis to guarantee that the density matrix used in the SSAdNDP procedure would accurately represent the original plane wave results. The bond orders were computed by the CHARGEMOL program using Manz's bond-order equation with DDEC6 partitioning [53,54] and are given in the Supplemental Material [55]. The band structures and molecular orbital diagrams are also obtained using the extended Huckel theory (eHT) YAEHMOP code [56]. Additional methodological details for the USPEX, VASP, and PHONOPY calculations are provided in Sec. S1 of the Supplemental Material [55].

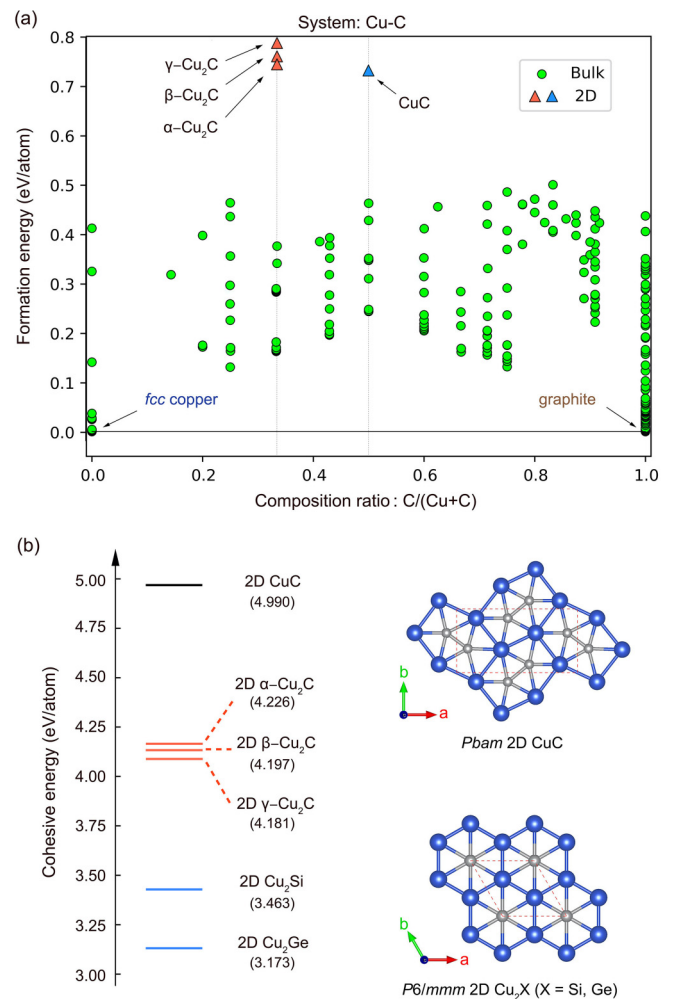


FIG. 1. (a) Formation energy (with respect to fcc copper and graphite at 0 K and 1 atm) of the most stable crystalline  $\text{Cu}_x\text{C}_y$  phases. Here, the convex hull of the Cu-C system is set at  $\Delta H_f = 0$  eV/atom. Green circles denote different bulk structures, i.e., stationary points on the PES. Those located above the convex hull are thermodynamically metastable. The red triangles indicate our three predicted two-dimensional dynamically stable  $\text{Cu}_2\text{C}$  structures, while the blue triangle depicts the published 2D CuC monolayer [27]. (b) Cohesive energies of previously reported and our predicted isoelectronic 2D  $\text{Cu}_2\text{X}$  compounds ( $X = \text{C}, \text{Si}$  [22,23], and  $\text{Ge}$  [25]) and the CuC monolayer [27]. Their structures are sketched on the right (copper, large blue circle; main group elements, small gray circle) with the associated space groups.

### III. RESULTS AND DISCUSSION

#### A. Stabilities of predicted 2D $\text{Cu}_2\text{C}$ phases

Our *in silico* CSP EA searches of 2D  $\text{Cu}_2\text{C}$  leads to the three most stable structures, namely,  $\alpha$  ( $P2/a$  space group),  $\beta$  ( $P2/m$  space group), and  $\gamma$  ( $Pm\bar{m}$  space group), which correspond to thermodynamically metastable phases with a positive formation enthalpy at  $P = 1$  atm and  $T = 0$  K, as shown in Fig. 1(a). Nevertheless, in materials sciences, thermodynamics is not the only criteria which governs the existence for a given compound. Kinetics is also a (or the) key factor, e.g., depending on the precursors and reactants. Kinetics may prevent

the decomposition of such a metastable phase if high activation barriers exist, i.e., the structure locates in a deep hole of the potential energy surface (PES). The carbon fullerene family illustrates this purpose:  $\text{C}_{60}$  buckminsterfullerene lies 0.383 eV/atom above ground-state graphite under ambient conditions [57]. The dynamical stabilities of our predicted 2D  $\text{Cu}_2\text{C}$  phases are confirmed by the absence of any imaginary frequencies of phonon dispersions in the entire Brillouin zone. Moreover, the *sine qua non* condition of a “viable” [58] compound is also verified by doing AIMD simulations at different temperatures (up to 1250 K) to verify that the proposed 2D  $\text{Cu}_2\text{C}$  phases are kinetically and thermally stable (see the phonon dispersions and AIMD simulations in the Supplemental Material [55]). Furthermore, considering that the transition metal atoms may induce magnetism in materials [59–61], the magnetism was checked to determine the preferred magnetic ground for our 2D  $\text{Cu}_2\text{C}$ , as presented in Table S1 of the Supplemental Material [55]. All 2D  $\text{Cu}_2\text{C}$  phases are nonmagnetic.

To evaluate the energetic stability of these layers, we calculated the cohesive energy  $E_{\text{coh}}$  using the following formula:

$$E_{\text{coh}} = \frac{2E_{\text{Cu}} + E_{\text{C}} - E_{\text{Cu}_2\text{C}}}{3}, \quad (1)$$

where  $E_{\text{Cu}_2\text{C}}$  is the total energy of 2D  $\text{Cu}_2\text{C}$ ,  $E_{\text{Cu}}$  and  $E_{\text{C}}$  are the energy of an isolated Cu and C atom, respectively. The cohesive energies of predicted  $\text{Cu}_2\text{C}$  phases are 4.226, 4.197, and 4.181 eV/atom, respectively. Our phases are ranked in energy in Fig. 1(b), as well as the other reported copper-based 2D materials, with their crystal structure captions. Compared with the previously computationally predicted [22] and then experimentally fabricated [23] 2D monolayer crystals  $\text{Cu}_2\text{Si}$  ( $E_{\text{coh}} = 3.463$  eV/atom),  $\text{Cu}_2\text{Ge}$  [25] ( $E_{\text{coh}} = 3.173$  eV/atom), and  $\text{CuC}$  [27] ( $E_{\text{coh}} = 4.990$  eV/atom), we notice that the cohesive energies of our selected phases are higher than those of  $\text{Cu}_2\text{Ge}$  and  $\text{Cu}_2\text{Si}$  monolayers. This indicates the viable thermodynamic stability of our proposed  $\text{Cu}_2\text{C}$  phases. Note that their formation energies are 0.755, 0.764, and 0.789 eV/atom, respectively. These positive values of the formation energies indicate their endothermic nature in experimental preparation. Note that silicene (2D Si) has a calculated formation energy of 0.7 eV/atom, but has been characterized on Ag (111) [62,63]. Thus, our predicted 2D slab ( $\alpha$ - $\text{Cu}_2\text{C}$ ) and monolayers ( $\beta$  and  $\gamma$ - $\text{Cu}_2\text{C}$ ) might be stabilized on theoretically designed substrates, a study which is beyond the present scope.

Meanwhile, the crystal structures of previously reported  $\text{Cu}_2\text{X}$  ( $X = \text{Si}$  and  $\text{Ge}$ ) and  $\text{CuC}$  monolayers are presented in the right panel of Fig. 1(b).  $\text{Cu}_2\text{X}$  ( $X = \text{Si}$  and  $\text{Ge}$ ) were predicted as a sixfold symmetric 2D material where each Si or Ge atom is coordinated to six Cu atoms to form a planar hexacoordinate silicon or germanium structure. Notably,  $\text{Cu}_2\text{Si}$ -type  $\text{Cu}_2\text{C}$  is also predicted in our structure searches, but is dynamically unstable (see the phonon dispersion in Section S4 of the Supplemental Material [55]). Moreover, the 2D  $\text{CuC}$  monolayer contains planar pentacoordinate carbon, where  $\text{C}_2$  dimers are embedded into Cu six-membered rings; such  $\text{C}_2@_{\text{Cu}_6}$  subunits are also detected in our 2D  $\beta$ - $\text{Cu}_2\text{C}$ .

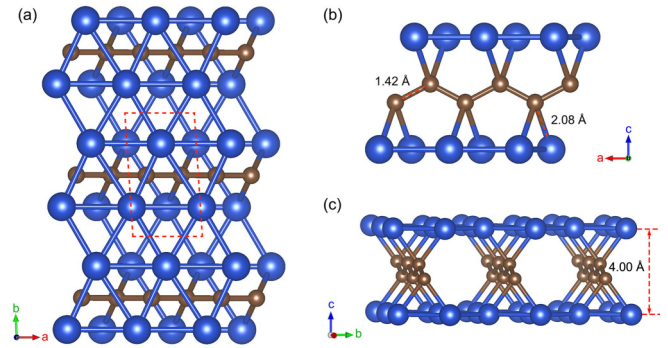


FIG. 2. 2D crystal structure of  $\alpha$ - $\text{Cu}_2\text{C}$  (space group:  $P2_1/a$ , No. 13;  $Z = 2$ ). (a) A view perpendicular to the slab. The monoclinic ( $\gamma = 92.6^\circ$ , pseudotetragonal) unit cell is highlighted. (b) A side view of the  $\text{Cu}_2\text{C}$  slab, the 1D zigzag poly- $(\text{C}_2)$  chains are sandwiched by two hexagonal Cu monolayers. (c) A tilted view.

## B. Geometrical, bonding, and electronic properties of 2D $\text{Cu}_2\text{C}$ phases

As mentioned previously, our EA searches of 2D  $\text{Cu}_2\text{C}$  polymorphs have led to three low-lying structures, namely,  $\alpha$  ( $P2_1/a$ , SG 13),  $\beta$  ( $P2_1/m$ , SG 10), and  $\gamma$  ( $Pm\bar{m}$ , SG 51) phases. Their optimized crystallographic parameters are given in Table S1 and discussed thereafter. To deeply analyze their bonding and electronic properties, we computed band structures, total and projected DOS, SSA $\bar{\text{N}}\text{D}\bar{\text{P}}$ , COHP, ELF, and bond orders of each 2D  $\text{Cu}_2\text{C}$  phase (see details in the Supplemental Material [55]). In the following, each of the three characterized 2D  $\text{Cu}_2\text{C}$  phases is discussed.

### 1. $\alpha$ phase: A $\text{Cu}_2\text{C}$ slab with sandwiched 1D zigzag carbon chains

After extensive 2D EA CSP searches,  $\alpha$ - $\text{Cu}_2\text{C}$  is predicted to be the ground state. Its crystal structure is displayed in Fig. 2 from different views and presents an unusual chemical topology. In  $\alpha$ - $\text{Cu}_2\text{C}$ , the C atoms form buckled carbon chains. This planar polymer is sandwiched by two hexagonal-close-packed (hcp) copper monolayers. Each trigonal planar carbon is connected to two carbon atoms at 1.42 Å, characteristic of a single/double bond character (1.42 Å in molecular aromatic benzene at PBE level). C-C-C valence bond angles of  $123.2^\circ$  are computed along the carbon chain, as expected for the  $sp^2$  atom type. Note that this 1D zigzag chain presents no short- and long-bond alternation along the carbon backbone, suggesting the  $\pi$  electrons are fully delocalized over the 1D organic chain. Such isostructural chains are encountered in  $\text{Li}_2\text{Ga}$  [64],  $\text{CaSi}$  [65], and  $\text{CrB}$ , among others [66]. In  $\alpha$ - $\text{Cu}_2\text{C}$ , the peculiar structural feature comes from the sandwiched carbon chains by two copper monolayers. A long separation (3.98 Å) between the two hcp Cu monolayers prevents any metal-metal bonding. Each carbon atom bridges two copper atoms ( $d_{\text{Cu-C}} = 2.09$  Å), ensuring the cohesion between metallic hcp Cu monolayers and organic polymeric net. Within each monolayer, the shortest Cu-Cu separations range from 2.46 to 2.69 Å (2.57 Å in bulk fcc copper and 2.41 Å in 2D hcp Cu monolayer).

The observed structure of 2D  $\alpha$ - $\text{Cu}_2\text{C}$  can be understood on the basis of the partitioning of a metallic and an organic



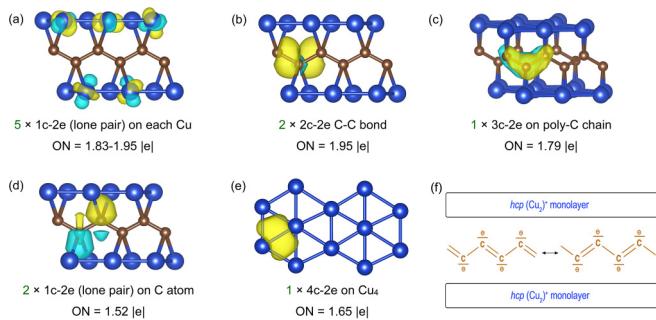


FIG. 3. SSAdNDP bonding patterns of  $\alpha$ -Cu<sub>2</sub>C: (a) five *d*-type lone pairs on each Cu atom, (b) two 2c-2e  $\sigma$ -bonds found between two C atoms, (c) a 3c-2e  $\pi$  bond on each of the bent C<sub>3</sub>, (d) two lone pairs on two C atoms, and (e) a 4c-2e  $\sigma$ -bond on Cu<sub>4</sub> rhombus, (f) Resonant Lewis structures of 1D (C<sub>2</sub><sup>2-</sup>)<sub>x</sub> chain. Each hcp copper monolayer is formally positively charged in this ionic model: (Cu<sub>2</sub>)<sup>+</sup>, i.e., delocalized Cu<sup>+</sup>(I) 3*d*<sup>10</sup> and Cu(0) 3*d*<sup>10</sup>4*s*<sup>1</sup> centers.

polymeric net, keeping in mind that some copper-carbon bonding interactions are at work in this metal-organic slab. Thus, electropositive elements, here copper, tend to transfer their valence electrons (or part of them) to the carbon framework. How many electrons are formally given by Cu monolayers to polycarbide chains? To answer, we employed the SSAdNDP method to rationalize the localized and multicentered bonding in the  $\alpha$ -Cu<sub>2</sub>C phase (see Fig. 3). There are four Cu (3*d*<sup>10</sup>4*s*<sup>1</sup>) and two C (2*s*<sup>2</sup>2*p*<sup>2</sup>) per unit cell, thus 52 valence electrons, i.e., 26 pairs of electrons to distribute into a tetragonal (Cu<sub>4</sub>C<sub>2</sub>) repeating unit. Concerning each hcp copper monolayer, our SSAdNDP analysis revealed five *d*-type lone pairs per Cu center (3*d*<sup>10</sup>) with occupation number (ON) values ranging from 1.83 to 1.95 |*e*| [see Fig. 3(a)], and thus here 20 pairs over 26 are localized on copper sites. One 2c-2e contact between two C atoms is identified along the 1D carbon chain with ON = 1.95 |*e*| corresponding to the expected  $\sigma$ (C-C) bond [see Fig. 3(b)]. Thus, two  $\sigma$  bonds per unit cell are assigned; moreover, a 3c-2e bond per bent C<sub>3</sub> unit is found with ON = 1.79 |*e*| [Fig. 3(c)], associated with a delocalized  $\pi$ (C-C) bond along the zigzag carbon chain, i.e., one  $\pi$  bond per C<sub>2</sub> repeating unit. To summarize, three bonding pairs at each carbon are identified: two  $\sigma$  and one  $\pi$ , as in delocalized cyclic C<sub>6</sub>H<sub>6</sub> benzene and polyacetylene (CH)<sub>x</sub>, in agreement with the single/double bond character of C-C separation (1.42 Å). Finally, a 1c-2e bond is located on each C atom with ON = 1.52 |*e*| and may be formally associated with a lone pair, shown in Fig. 3(d). These lone pairs bring the total of electrons to 8 per carbon atom (octet rule) within the organic conjugated chain. In 2D  $\alpha$ -Cu<sub>2</sub>C, each C has formally a minus charge, i.e., poly-(C<sub>2</sub><sup>2-</sup>) with a 10-valence-electron repeat unit. This 1D planar zigzag poly-(C<sub>2</sub><sup>2-</sup>) chain may be viewed as a deprotonated polyacetylene [see its Lewis structures displayed in Fig. 3(f)]. Each carbon is bent, as expected for valence shell electron-pair repulsion (VSEPR) AX<sub>2</sub>E configuration.

Summarizing the assigned electron pairs, one counts 25 pairs per (Cu<sub>4</sub>C<sub>2</sub>) unit, namely, 5 per Cu atom and 5 per C<sub>2</sub> motifs (2  $\sigma$ , 1  $\pi$ , and 2 lone pairs). From a localized perspective, 2 Cu atoms over 4 metal atoms gives their 4*s*<sup>1</sup> electrons

to each C<sub>2</sub> motif, leading to the ionic picture [(Cu<sub>4</sub><sup>2+</sup>)(C<sub>2</sub><sup>2-</sup>)]. Thus, over 26 electron pairs of the Cu<sub>4</sub>C<sub>2</sub> repeat unit, it remains one pair of electrons per Cu<sub>4</sub>C<sub>2</sub> unit which are delocalized over the slightly distorted hcp Cu monolayers of 2D  $\alpha$ -Cu<sub>2</sub>C as illustrated by a 4c-2e  $\sigma$ -bond with ON = 1.65 |*e*| on a Cu<sub>4</sub> rhombus, as shown in Fig. 3(e). This explains the slightly weaker Cu-Cu bond found in hcp copper positively charged monolayers—formally 2D (Cu<sub>2</sub><sup>+</sup>) in 2D  $\alpha$ -Cu<sub>2</sub>C [averaged integrated crystal orbital Hamiltonian population (ICOHP) (Cu-Cu) = -0.54 and -0.64 eV/pair in  $\alpha$ -Cu<sub>2</sub>C and 2D hcp Cu monolayers [67], respectively].

The resulting bonding patterns are consistent with classical chemical rules, i.e., oxidation number, octet rules, Lewis resonant structures, and VSEPR theory: in an ionic formulation 2D  $\alpha$ -Cu<sub>2</sub>C may be seen as (Cu<sub>2</sub><sup>+</sup>)(C<sub>2</sub><sup>-</sup>) or (Cu<sub>4</sub><sup>2+</sup>)(C<sub>2</sub><sup>2-</sup>) per unit. Topology, bonding, and charge partitioning properties confer to 2D  $\alpha$ -Cu<sub>2</sub>C a specific peculiarity: the coordination of an ionic lattice poly-(C<sub>2</sub><sup>2-</sup>) host by a metal framework (here two Cu<sub>2</sub><sup>+</sup> monolayers in 2D  $\alpha$ -Cu<sub>2</sub>C). Thus, the arrangement of donor and acceptor sites is opposite to that occurring in conventional coordination compounds, i.e., coordination of the cation by a Lewis base as illustrated in molecular ferrocene Fe( $\eta$ <sup>5</sup>-C<sub>5</sub>H<sub>5</sub>)<sub>2</sub> where Fe<sup>2+</sup> is sandwiched by two anionic cyclopentadienyl rings (C<sub>5</sub>H<sub>5</sub>)<sup>-</sup>. One may consider our predicted 2D  $\alpha$ -Cu<sub>2</sub>C has an inverse coordination 2D crystal [68].

What about the electronic performance of 2D  $\alpha$ -Cu<sub>2</sub>C? The DFT calculations were executed to investigate the band structure and the accordingly total and projected DOS, as displayed in Fig. 4. Starting from lower energies, the first feature in the band structure and DOS appears between -4 eV and  $\sim$ -2 eV, a strong DOS peak with mainly copper *d* orbital in character, which shows a typical signature of a transition metal (2D and 3D nets [67]). These *d* bands are fully occupied (*d*<sup>10</sup>). The second noticeable aspect of the DOS is the computed low density of states at  $\sim$ -0.3 eV; the copper bands are highly dispersed in this energy region, as shown in its band structure [Fig. 4(a)]. The Fermi level crosses this low DOS, and 2D  $\alpha$ -Cu<sub>2</sub>C *P2/a* is metallic. Finally, the third characteristic is the presence of the carbon 2*p*-based band crossings (labeled as L<sub>*i*</sub>, *i* = 1, 2, and 3) in the vicinity of the Fermi level [see the inset in Fig. 4(a)]. These carbon 2*p*-based branches correspond to the bonding  $\pi_{CC}$  and antibonding  $\pi_{CC}^*$  based crystalline orbitals. They are well-dispersed along the  $\Gamma \rightarrow Z$  path, i.e., along the carbon chain direction (*a* lattice). At Z ( $\frac{1}{2}$ , 0), these  $\pi_{CC}$  and  $\pi_{CC}^*$  bands are degenerate and 2*p*-2*p* nonbonding in nature (see our detailed orbital analysis in the Supplemental Material [55]). Such a feature is expected in a 1D chain model which contains two atoms and two orbitals per cell, with equidistant interatomic separation. Furthermore, in Z (0,  $\frac{1}{2}$ )  $\rightarrow$  C ( $\frac{1}{2}$ ,  $\frac{1}{2}$ ), these  $\pi$  and  $\pi^*$  nonbonding orbitals interact with copper orbitals (mainly *s/p* Cu orbitals, see in Fig. S15), and are slightly stabilized. Note that stabilization for  $\pi$  and  $\pi^*$  are not expected to be equivalent, thus degeneracy is lost along the Z  $\rightarrow$  C *k*-path. This is retrieved in the computed band structure.

For further understanding the band dispersion and for a clear illustration of the carbon 2*p*-based band crossings, the 3D band structure is displayed in Fig. 4(c). We can see that

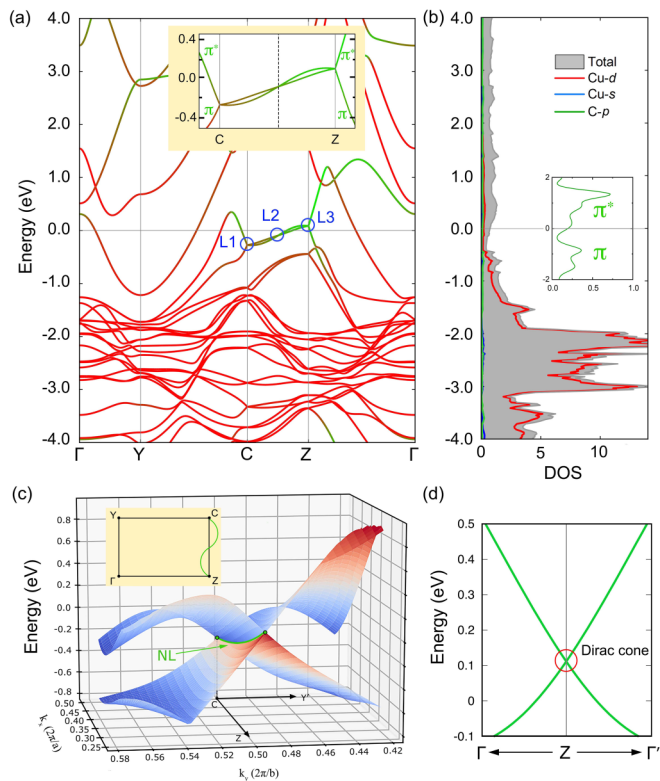


FIG. 4. (a) Band structure for  $\alpha\text{-Cu}_2\text{C}$ , the colored bands indicate the atomic contributions to the band structure, from red (high Cu contributions) to green (high C contribution). The inset is a zoom-in of bands near the Fermi level. (b) Total and partial DOS (pDOS), underlying the contributions of Cu  $d$  orbitals (red), Cu  $s$  orbitals (blue), and C  $p$  orbitals (green). The inset shows the pDOS of C- $\pi$  orbital in the energy range of  $-2$  and  $2$  eV, the bonding ( $\pi$ ) and antibonding ( $\pi^*$ ) parts are indicated. (c) Three-dimensional band structure showing the Dirac nodal line. The inset is a schematic of the nodal line in the first Brillouin zone. (d) Enlarged band structure around the high symmetry point  $Z$ . The Dirac cone is indicated. The Fermi level is set at  $0$  eV.

$L_i$  ( $i = 1, 2$ , and  $3$ ) are not isolated band crossings, but in fact they are connected together to form a quasi-1D Dirac nodal line along  $C \rightarrow Z$  in the first Brillouin, as illustrated in the inset of Fig. 4(c). By artificially changing the crystal configuration (maintain or break certain spatial symmetry) to evaluate the symmetry-related property of Dirac nodal lines, it was confirmed that such 1D Dirac nodal lines are protected by the glide plane symmetry in  $\alpha\text{-Cu}_2\text{C}$  (see Supplemental Material [55]). Dirac nodal ring features are widely investigated in 2D copper-based materials, such as  $\text{Cu}_2\text{Si}$  [24],  $\text{Cu}_2\text{Ge}$  [26], and  $\text{CuSe}$  [29]. However, 1D nodal lines are extremely rare. This structure is an example of 2D copper compounds featuring a 1D nodal line.

The Dirac cone-like electronic state generally produces excellent electronic transport properties. As shown in Fig. 4(d), the bands along the  $k_x$  direction ( $\Gamma \rightarrow Z \rightarrow \Gamma'$ ) feature a Dirac cone, which exhibits a linear dispersion. Therefore, the Fermi velocity ( $v_f$ ) was obtained by using the expression  $v_f = \frac{\partial(E)}{\hbar\partial(k)}$ , where the  $\frac{\partial(E)}{\partial(k)}$  is the slope of the linear band, and  $\hbar$  is the reduced Planck's constant. The calculated  $v_f$  value is

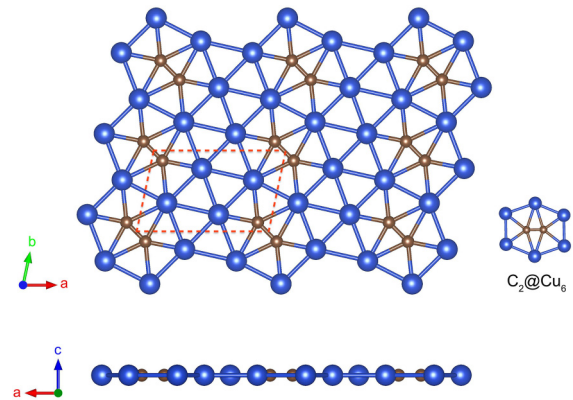


FIG. 5. (a) Top and side view of the 2D crystal structure of  $\beta\text{-Cu}_2\text{C}$ . The red dashed line indicates the  $(\text{Cu}_4\text{C}_2)$  repeat unit cell, and the  $\text{C}_2@Cu_6$  subunit is depicted.

$2.45 \times 10^5$  m/s, which is comparable to the values of  $\text{Na}_3\text{Bi}$  ( $2.43 \times 10^5$  m/s) [69] and  $\text{Bi}_2\text{Se}_3$  [ $(3.4 \pm 0.3) \times 10^5$  m/s] [70], and smaller than that in graphene ( $8.22 \times 10^5$  m/s) [71]. According to the definition of the effective mass of the charge carriers  $m^* = \hbar^2 \left[ \frac{d^2E(k)}{dk^2} \right]^{-1}$ , the linear dispersion of the energy bands suggests close to zero effective mass for the carriers near the Fermi level. Therefore,  $\alpha\text{-Cu}_2\text{C}$  is expected to have ultrahigh carrier mobility.

## 2. $\beta$ phase: a $\text{Cu}_2\text{C}$ monolayer with embedded $\text{C}_2$ dimers

2D  $\beta\text{-Cu}_2\text{C}$  crystallizes in the monoclinic  $P2/m$  space group (SG 10,  $Z = 2$ ). Its structure is displayed in Fig. 5.

Here, a ppC-containing copper carbide monolayer is identified on the PES of  $\text{Cu}_2\text{C}$  as a local minimum, i.e., no imaginary frequency appears in its phonon dispersion curve. The 2D  $\beta\text{-Cu}_2\text{C}$  structure can be viewed as a distorted hcp copper monolayer embedding molecular-like  $\text{C}_2$  units. Each dicarbide dumbbell is encapsulated in a six-membered copper ring (see inset of Fig. 5). This  $\text{C}_2@Cu_6$  subunit presents the same motif that is the one reported in 2D  $\text{CuC}$  [27]. The interatomic distance in  $\text{C}_2$  is computed at  $1.31 \text{ \AA}$  and features a double-bond character, which is confirmed by a calculated Manz CC bond order of  $1.97$  (see details in the Supplemental Material [55]). The Cu-C bond distances are calculated at  $1.94$  and  $2.14 \text{ \AA}$  with a bond order of  $0.74$  and  $0.55$ , respectively. Meanwhile, the calculated ELF plots also reflect a moderate covalent bonding character between  $\text{C}_2$  units and copper centers (see Fig. S14 in the Supplemental Material [55]). Moreover, Cu-Cu separations range from  $2.38$  to  $2.58 \text{ \AA}$  ( $2.41 \text{ \AA}$  in 2D hcp Cu). This Cu-Cu weakening reflects the charge transfer from the copper framework to the  $\text{C}_2$  units.

The interatomic C-C COHP of 2D  $\beta\text{-Cu}_2\text{C}$  is displayed in the left panel of Fig. 6(c). Its main peaks could be assigned to a given bonding, nonbonding, or antibonding molecular orbital level of discrete  $\text{C}_2$  species [72,73] [see the right panel of Fig. 6(c)]. Looking at the occupied C-C levels, one may clearly see that the filling of the nonbonding  $1\sigma_g$  level and the half filling of the two antibonding  $1\pi_g^*$  orbitals of  $\text{C}_2$  lead to a formal charge of  $-4$  per  $\text{C}_2$ , indeed resulting in a double bond (6 valence electrons in bonding  $1\sigma_g$  and  $1\pi_u$  levels and 2 valence electrons in degenerated antibonding

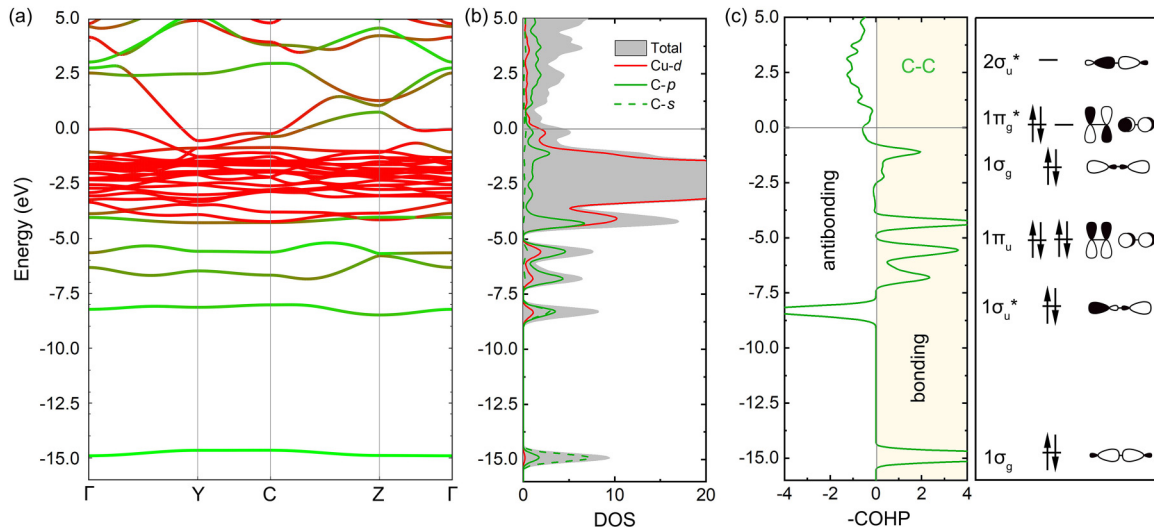


FIG. 6. (a) Band structure for  $\beta$ -Cu<sub>2</sub>C, the colored bands indicate the atomic contributions to the band structure, from red (high Cu contributions) to green (high C contribution). (b) Total and partial DOS. (c) The left part is the crystal orbital Hamiltonian population (COHP) for C-C interaction, and the right part shows a schematic molecular orbital energy level diagram of the C<sub>2</sub><sup>4-</sup> unit. The Fermi level is set at 0 eV.

$1\pi_g^*$ ; the 12-valence-electron C<sub>2</sub><sup>4-</sup> species is isoelectronic to the O<sub>2</sub> species). Thus,  $\beta$ -Cu<sub>2</sub>C may be viewed as containing four monocations Cu<sup>+</sup> and C<sub>2</sub><sup>4-</sup> motifs per repeat unit, (Cu<sup>+</sup>)<sub>4</sub>(C<sub>2</sub><sup>4-</sup>).

From the PBE band structures and the DOS of  $\beta$ -Cu<sub>2</sub>C displayed in Figs. 6(a) and 6(b), respectively, it can be seen that the Fermi level crosses a low density of states; this feature indicates a semimetallic character. To confirm this, the atom-projected DOS is recomputed using the hybrid HSE06 functional (see Fig. S8 in the Supplemental Material [55]), which also shows such a semimetallic character for  $\beta$ -Cu<sub>2</sub>C.

### 3. $\gamma$ phase: A Cu<sub>2</sub>C monolayer with embedded 1D zigzag carbon chains

Our 2D evolutionary searches uncovered  $\gamma$ -Cu<sub>2</sub>C as the third low-lying energy static metastable phase located at 25 meV/atom above the 2D  $\alpha$ -Cu<sub>2</sub>C. It crystallizes in the orthorhombic *Pmm* space group (SG 51, Z = 2). Its crystal structure is shown in Fig. 7. Two-dimensional  $\gamma$ -Cu<sub>2</sub>C is a planar-tetracoordinate-C-containing monolayer, which contains 1D zigzag carbon chains connecting each two hexagonal planar copper ribbons. The organic motif poly-(C<sub>2</sub>) is topologically analog to the one found in 2D  $\alpha$ -Cu<sub>2</sub>C, but embedded in the plane of the metal monolayer. There are one C site and two inequivalent Cu sites in the primitive unit cell, i.e., Cu<sub>4</sub>C<sub>2</sub> subunit per cell (see Fig. 7). Each C atom binds with two neighboring C atoms at 1.38 Å (single/double bond character) and two Cu atoms at 2.13 Å. Here, the Cu<sub>4</sub>C<sub>2</sub> motif is planar instead of tetrahedral as found in  $\gamma$ -Cu<sub>2</sub>C. A C-C-C valence bond angle of 127.3° is computed along the zigzag carbon chain. To rationalize the observed bonding mode in poly-(C<sub>2</sub>), one may consider an electron charge transfer from electropositive copper, i.e., (Cu<sub>4</sub>)<sup>2+</sup>, to a dicarbide repeating unit C<sub>2</sub><sup>2-</sup>. Effectively, a polyacetylene-like chain (C<sub>2</sub><sup>2-</sup>)<sub>x</sub> presents the AX<sub>2</sub>E center, i.e., bent configuration from VSEPR rule, and regular CC bonds of formally 1.5 bond order. This formal charge assignment based on a crude ionic

model is in agreement with the calculated CC bond order of 1.43. Moreover, the delocalized  $\pi$  character along the organic chain is confirmed by the analysis of the band structure of the 2D  $\gamma$ -Cu<sub>2</sub>C monolayer displayed in Fig. 8(a); the Fermi level crosses two degenerated carbon 2*p*-based bands, namely, bonding  $\pi_{CC}$  and antibonding  $\pi_{CC}^*$  at both *S*( $\frac{1}{2}, \frac{1}{2}$ ) and *Y*( $\frac{1}{2}, 0$ ) *k*-points of the Brillouin zone. The expected Peierls distortion, i.e., alternating short and long CC bonds along the 1D zigzag poly-(C<sub>2</sub><sup>2-</sup>) chain and gap opening, does not appear due to copper-carbon bonding interactions which prevent any structural deformation. Finally, the delocalized (metallic) character among hexagonal planar copper ribbons is confirmed by both SSA NDP and ELF results (see Supplemental Material [55]).

From this peculiar topological feature, i.e., the presence of a 1D zigzag carbon chain, one may expect a Dirac nodal line in the  $\gamma$ -Cu<sub>2</sub>C band structure. A close inspection of its band structure reveals a 1D Dirac nodal line along *S* → *Y* in the first Brillouin zone, which is similar to the one observed in  $\alpha$ -Cu<sub>2</sub>C. As discussed above, the  $\pi_{CC}$  and  $\pi_{CC}^*$  bands of

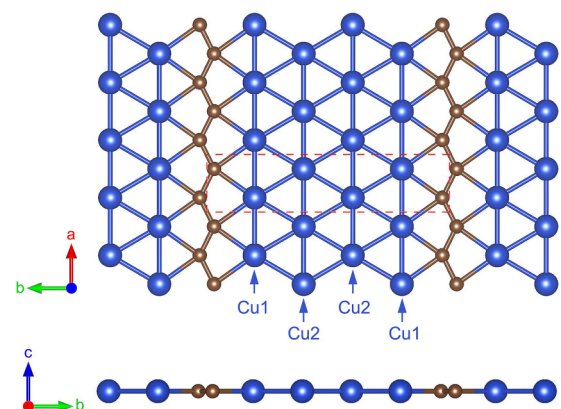


FIG. 7. Top and side views of 2D crystal structure for  $\gamma$ -Cu<sub>2</sub>C. The red dashed line indicates the unit cell, and two inequivalent Cu sites are indicated by Cu1 and Cu2.



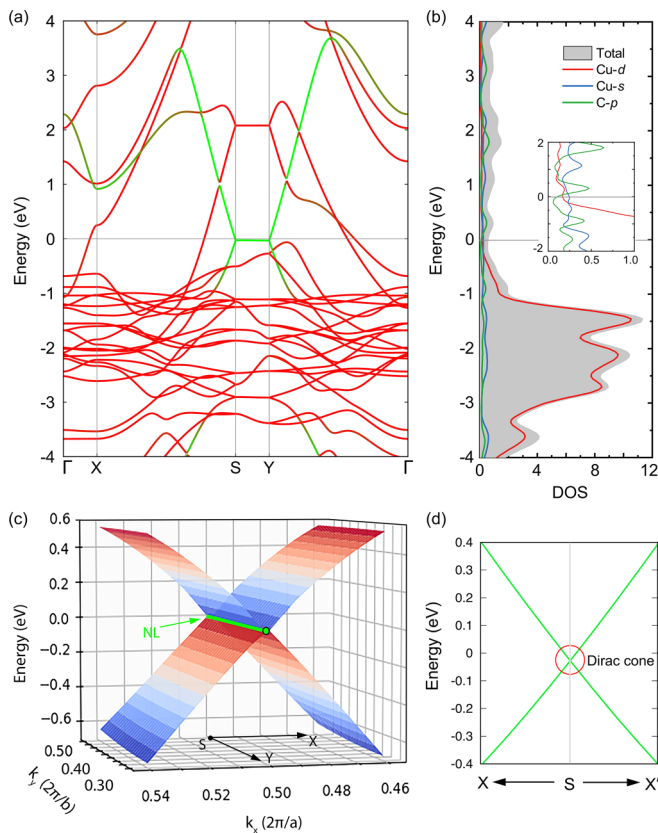


FIG. 8. (a) Band structure for  $\gamma\text{-Cu}_2\text{C}$ . The colored bands indicate the atomic contributions to the band structure, from red (high Cu contributions) to green (high C contribution). (b) Total and partial DOS, underlying the contributions of Cu  $d$  orbitals (red), Cu  $s$  orbitals (blue), and C  $p$  orbitals (green). The inset shows the pDOS in the energy range of  $-2$  and  $2$  eV. (c) Three-dimensional band structure showing the Dirac nodal line. (d) Enlarged band structure around the high symmetry point  $S$ . The Dirac cone is indicated. The Fermi level is set at  $0$  eV.

the polyacetylene-like structure meet at the Fermi level from the  $S \rightarrow Y$  path ( $ab$  plane in direct space). These nonbonding degenerated bands are purely carbon in character in this Brillouin zone section. By symmetry, the mixture of Cu orbitals with C ( $2p$ ) ones is not allowed in the range  $S \rightarrow Y$ . This explains the straight nodal line shown in a 3D band structure along  $S \rightarrow Y$  in Fig. 8(c). Based on the computed total and projected DOS (PBE and HSE06), 2D  $\gamma\text{-Cu}_2\text{C}$  is metallic with the Fermi-level-crossing low density of states (see S7 in the Supplemental Material [55]). To summarize,

the  $\gamma\text{-Cu}_2\text{C}$  also exhibits the Dirac cone-like electronic state with a linear dispersion, as shown in Fig. 8(d). Moreover, the Fermi velocity ( $v_f$ ) was calculated as  $3.85 \times 10^5$  m/s, which is even higher than that of  $\alpha\text{-Cu}_2\text{C}$  ( $2.45 \times 10^5$  m/s),  $\text{Na}_3\text{Bi}$  ( $2.43 \times 10^5$  m/s) [69], and  $\text{Bi}_2\text{Se}_3$  [ $(3.4 \pm 0.3) \times 10^5$  m/s] [70] and is approximately half of that of graphene ( $8.22 \times 10^5$  m/s) [71]. Therefore, the 2D  $\gamma\text{-Cu}_2\text{C}$  is also expected to be a promising 2D candidate which has ultrahigh carrier mobility.

#### IV. CONCLUSION

In summary, by *ab initio* evolutionary algorithm searches, first-principle calculations, and molecular dynamics simulations, we predicted three two-dimensional  $\text{Cu}_2\text{C}$  compounds, which are kinetically stable. The global minimum  $\alpha\text{-Cu}_2\text{C}$  is an exciting new structure and has been identified to be an ionocovalent compound consisting of 1D zigzag carbon chains and two hexagonal-close-packed copper monolayers playing the roles of anions and cations. Two-dimensional  $\alpha\text{-Cu}_2\text{C}$  belongs to the family of inversion coordination compounds. Moreover,  $\beta\text{-Cu}_2\text{C}$  is a planar-pentacoordinate-carbon-containing monolayer, where each C atom binds with four Cu atoms and one neighboring C atom forming a  $\text{C}_2\text{@Cu}_6$  subunit in the same plane. Furthermore,  $\gamma\text{-Cu}_2\text{C}$  is a planar-tetracoordinate-carbon-containing monolayer, which also presents 1D zigzag carbon chains, connecting each two hexagonal planar copper ribbons. Remarkably, the  $\alpha$ - and  $\gamma\text{-Cu}_2\text{C}$  phases are reported as 1D Dirac nodal line materials with high Fermi velocity among copper-based 2D structures. Fermi velocities ( $v_f$ ) as high as  $2.45 \times 10^5$  and  $3.85 \times 10^5$  m/s are calculated for  $\alpha$ - and  $\gamma\text{-Cu}_2\text{C}$  phases, respectively. This work is an effective effort to design and stabilize 2D copper carbide layers with an exotic structure and a Dirac nodal line. We expect that our findings will inspire the materials science community to synthesize our *in silico* proposed 2D  $\text{Cu}_2\text{C}$  layers.

#### ACKNOWLEDGMENTS

We thank the ANR PRCI Predict\_2D\_Nanomat (PI G.F.), the FEDER, and the Nouvelle Aquitaine Region (France). We also acknowledge the High-Performance Computing Centers of Poitiers University Mésocentre SPIN, France) and the Irène KNL/TGCC, and we acknowledge Jean Zay/IDRIS GENCI (France) under Project No. X2016087539 and the Jean Zay Challenge 2019 for allocation of computing time. Thanks to our colleagues Dr. Frédéric Guégan, Dr. Somayeh Faraji Nafchi, and Rabii Larhlami of the Applied Quantum Chemistry group at E4-IC2MP for proofreading and constructive criticism of this manuscript.

- [1] K. S. Novoselov, A. K. Geim, S. V. Morozov, D. Jiang, Y. Zhang, S. V. Dubonos, I. V. Grigorieva, and A. A. Firsov, *Science* **306**, 666 (2004).
- [2] A. H. Castro Neto, F. Guinea, N. M. R. Peres, K. S. Novoselov, and A. K. Geim, *Rev. Mod. Phys.* **81**, 109 (2009).
- [3] A. K. Geim and K. S. Novoselov, *Nat. Mater.* **6**, 183 (2007).

- [4] G. W. Semenoff, *Phys. Rev. Lett.* **53**, 2449 (1984).
- [5] K. S. Novoselov, A. K. Geim, S. V. Morozov, D. Jiang, M. I. Katsnelson, I. V. Grigorieva, S. V. Dubonos, and A. A. Firsov, *Nature (London)* **438**, 197 (2005).
- [6] Y. Lin, T. V. Williams, and J. W. Connell, *J. Phys. Chem. Lett.* **1**, 277 (2010).

- [7] W.-J. Ong, L.-L. Tan, Y. H. Ng, S.-T. Yong, and S.-P. Chai, *Chem. Rev.* **116**, 7159 (2016).
- [8] J. Zhang, Y. Chen, and X. Wang, *Energy Environ. Sci.* **8**, 3092 (2015).
- [9] H. Liu, Y. Du, Y. Deng, and D. Y. Peide, *Chem. Soc. Rev.* **44**, 2732 (2015).
- [10] V. Eswaraiah, Q. Zeng, Y. Long, and X. Liu, *Small* **12**, 3480 (2016).
- [11] B. Lalmi, H. Oughaddou, H. Enriquez, A. Kara, S. Vizzini, B. Ealet, and B. Aufray, *Appl. Phys. Lett.* **97**, 223109 (2010).
- [12] L. Tao, E. Cinquanta, D. Chiappe, C. Grazianetti, M. Fanciulli, M. Dubey, A. Molle, and D. Akinwande, *Nat. Nanotechnol.* **10**, 227 (2015).
- [13] M. Chhowalla, H. S. Shin, G. Eda, L.-J. Li, K. P. Loh, and H. Zhang, *Nat. Chem.* **5**, 263 (2013).
- [14] C. Tan and H. Zhang, *Chem. Soc. Rev.* **44**, 2713 (2015).
- [15] M. Naguib, V. N. Mochalin, M. W. Barsoum, and Y. Gogotsi, *Adv. Mater.* **26**, 992 (2014).
- [16] B. Anasori, M. R. Lukatskaya, and Y. Gogotsi, *Nat. Rev. Mater.* **2**, 16098 (2017).
- [17] V. M. H. Ng, H. Huang, K. Zhou, P. S. Lee, W. Que, J. Z. Xu, and L. B. Kong, *J. Mater. Chem. A* **5**, 3039 (2017).
- [18] X. Huang, S. Tang, X. Mu, Y. Dai, G. Chen, Z. Zhou, F. Ruan, Z. Yang, and N. Zheng, *Nat. Nanotechnol.* **6**, 28 (2011).
- [19] Z. Fan, X. Huang, C. Tan, and H. Zhang, *Chem. Sci.* **6**, 95 (2015).
- [20] J. Shamsi, Z. Dang, P. Bianchini, C. Canale, F. Di Stasio, X. Brescia, M. Prato, and L. Manna, *J. Am. Chem. Soc.* **138**, 7240 (2016).
- [21] S. Yang, W. Niu, A.-L. Wang, Z. Fan, B. Chen, C. Tan, Q. Lu, and H. Zhang, *Angew. Chem., Int. Ed.* **56**, 4252 (2017).
- [22] L. M. Yang, V. Bačić, I. A. Popov, A. I. Boldyrev, T. Heine, T. Frauenheim, and E. Ganz, *J. Am. Chem. Soc.* **137**, 2757 (2015).
- [23] B. Feng, B. Fu, S. Kasamatsu, S. Ito, P. Cheng, C.-C. Liu, S. K. Mahatha, P. Sheverdyaeva, P. Moras, M. Arita *et al.* *Nat. Commun.* **8**, 1007 (2017).
- [24] E. Unsal, F. Iyikanat, H. Sahin, and R. T. Senger, *RSC Adv.* **8**, 39976 (2018).
- [25] L. M. Yang, I. A. Popov, A. I. Boldyrev, T. Heine, T. Frauenheim, and E. Ganz, *Phys. Chem. Chem. Phys.* **17**, 17545 (2015).
- [26] L. Liu, C. Wang, J. Li, X.-Q. Chen, Y. Jia, and J.-H. Cho, *Phys. Rev. B* **101**, 165403 (2020).
- [27] C. Zhu, H. Lv, X. Qu, M. Zhang, J. Wang, S. Wen, Q. Li, Y. Geng, Z. Su, X. Wu, Y. Li, and Y. Ma, *J. Mater. Chem. C* **7**, 6406 (2019).
- [28] X. Lin, X. J. C. Lu, Y. Shao, Y. Y. Zhang, X. Wu, J. B. Pan, L. Gao, S. Y. Zhu, K. Qian, Y. F. Zhang, D. L. Bao, L. F. Li, Y. Q. Wang, Z. L. Liu, J. T. Sun, T. Lei, C. Liu, J. O. Wang, K. Ibrahim, D. N. Leonard *et al.*, *Nat. Mater.* **16**, 717 (2017).
- [29] L. Gao, J. T. Sun, J. C. Lu, H. Li, K. Qian, S. Zhang, Y. Y. Zhang, T. Qian, H. Ding, X. Lin, S. Du, and H. J. Gao, *Adv. Mater.* **30**, 1707055 (2018).
- [30] J. Nevalaita and P. Koskinen, *Nanoscale* **11**, 22019 (2019).
- [31] A. R. Oganov and C. W. Glass, *J. Chem. Phys.* **124**, 244704 (2006).
- [32] A. R. Oganov, A. O. Lyakhov, and M. Valle, *Acc. Chem. Res.* **44**, 227 (2011).
- [33] A. O. Lyakhov, A. R. Oganov, H. T. Stokes, and Q. Zhu, *Phys. Commun.* **184**, 1172 (2013).
- [34] X.-F. Zhou, X. Dong, A. R. Oganov, Q. Zhu, Y. Tian, and H.-T. Wang, *Phys. Rev. Lett.* **112**, 085502 (2014).
- [35] A. R. Oganov, Y. Ma, A. O. Lyakhov, M. Valle, and C. Gatti, *Rev. Mineralogy Geochemistry* **71**, 271 (2010).
- [36] G. Kresse and J. Furthmuller, *Phys. Rev. B* **54**, 11169 (1996).
- [37] G. Kresse and J. Furthmuller, *Comput. Mater. Sci.* **6**, 15 (1996).
- [38] P. E. Blochl, *Phys. Rev. B* **50**, 17953 (1994).
- [39] J. P. Perdew, K. Burke, and M. Ernzerhof, *Phys. Rev. Lett.* **77**, 3865 (1996).
- [40] J. Heyd, G. E. Scuseria, and M. Ernzerhof, *J. Chem. Phys.* **118**, 8207 (2003).
- [41] A. V. Krukau, O. A. Vydrov, A. F. Izmaylov, and G. E. Scuseria, *J. Chem. Phys.* **125**, 224106 (2006).
- [42] J. A. Pople, *Rev. Mod. Phys.* **71**, 1267 (1999).
- [43] S. Baroni, P. Giannozzi, and A. Testa, *Phys. Rev. Lett.* **58**, 1861 (1987).
- [44] S. Baroni, S. De Gironcoli, A. Dal Corso, and P. Giannozzi, *Rev. Mod. Phys.* **73**, 515 (2001).
- [45] X. Gonze, *Phys. Rev. A* **52**, 1096 (1995).
- [46] A. Togo, F. Oba, and I. Tanaka, *Phys. Rev. B* **78**, 134106 (2008).
- [47] A. Togo, L. Chaput, I. Tanaka, and G. Hug, *Phys. Rev. B* **81**, 174301 (2010).
- [48] G. J. Martyna, M. L. Klein, and M. Tuckerman, *J. Chem. Phys.* **97**, 2635 (1992).
- [49] M. Cococcioni and S. de Gironcoli, *Phys. Rev. B* **71**, 035105 (2005).
- [50] T. R. Galeev, B. D. Dunnington, J. R. Schmidt, and A. I. Boldyrev, *Phys. Chem. Chem. Phys.* **15**, 5022 (2013).
- [51] S. Maintz, V. L. Deringer, A. L. Tchougréeff, and R. Dronskowski, *J. Comput. Chem.* **37**, 1030 (2016).
- [52] A. Savin, R. Nesper, S. Wengert, and T. F. Fässler, *Angew. Chem., Int. Ed.* **36**, 1808 (1997).
- [53] T. A. Manz and D. S. Sholl, *J. Chem. Theory Comput.* **7**, 4146 (2011).
- [54] T. A. Manz and N. G. Limas, *RSC Adv.* **6**, 47771 (2016).
- [55] See Supplemental Material at <http://link.aps.org/supplemental/10.1103/PhysRevMaterials.5.034003> for an additional methodological details; variable composition evolutionary algorithm searches; calculated structural parameters, energies, and magnetisms for all predicted 2D Cu<sub>2</sub>C compounds; the energies and structure information of previously reported 2D Cu<sub>2</sub>Si, Cu<sub>2</sub>Ge, CuC, SiC, and SiC<sub>2</sub> are also presented; phonon dispersion curves; *abinitio* molecular dynamics simulations; DOS-HSE06; crystal overlap Hamilton population (COHP); DDEC6 bond order; electron localization function (ELF) contour plots; and orbital analysis and symmetry testing of the Dirac nodal line in the predicted  $\alpha$ -Cu<sub>2</sub>C.
- [56] G. Landrum, and W. Glassey, Viewkel is distributed as part of the YAeHMOP extended Huckel molecular orbital package, 2001, <http://Yaehmop.Sourceforge.Net>.
- [57] A. Jain, S. P. Ong, G. Hautier, W. Chen, W. D. Richards, S. Dacek, S. Cholia, D. Gunter, D. Skinner, G. Ceder, and K. Persson, *APL Mater.* **1**, 11002 (2013).
- [58] R. Hoffmann, *Am. Sci.* **75**, 619 (1987).
- [59] Y. Matsumoto, M. Murakami, T. Shono, T. Hasegawa, T. Fukumura, M. Kawasaki, P. Ahmet, T. Chikyow, S. Y. Koshihara, and H. Koinuma, *Science* **291**, 854 (2001).
- [60] B. Wang, Q. Lu, Y. Ge, K. Zhang, W. Xie, W. M. Liu, and Y. Liu, *Phys. Rev. B* **96**, 134116 (2017).



- [61] B. Wang, H. Gao, Q. Lu, W.H. Xie, Y. Ge, Y.-H. Zhao, K. Zhang, and Y. Liu, *Phys. Rev. B* **98**, 115164 (2018).
- [62] P. Vogt, P. De Padova, C. Quaresima, J. Avila, E. Frantzeskakis, M. C. Asensio, A. Resta, B. Ealet, and G. Le Lay, *Phys. Rev. Lett.* **108**, 155501 (2012).
- [63] A. K. Singh, K. Mathew, H. L. Zhuang, and R. G. Hennig, *J. Phys. Chem. Lett.* **6**, 1087 (2015).
- [64] P. Alemany, M. Llunell, and E. Canadell, *Inorg. Chem.* **44**, 374 (2005).
- [65] I. M. Kurylyshyn, T. F. Fässler, A. Fischer, C. Hauf, G. Eickerling, M. Presnitz, and W. Scherer, *Angew. Chem., Int. Ed.* **53**, 3029 (2014).
- [66] A. Vegas, *Struct. Chem.* **44**, 1635 (2016).
- [67] L.-M. Yang, T. Frauenheim, and E. Ganz, *J. Nanomater.* **2016**, 8429510 (2016).
- [68] I. Haiduc, *Coord. Chem. Rev.* **338**, 1 (2017).
- [69] Z. K. Liu, B. Zhou, Y. Zhang, Z. J. Wang, H. M. Weng, D. Prabhakaran, S.-K. Mo, Z. X. Shen, Z. Fang, X. Dai, Z. Hussain, and Y. L. Chen, *Science* **343**, 864 (2014).
- [70] Y. Xia, D. Qian, D. Hsieh, L. Wray, A. Pal, H. Lin, A. Bansil, D. Grauer, Y. S. Hor, R. J. Cava, and M. Z. Hasan, *Nat. Phys.* **5**, 398 (2009).
- [71] Z. Wang, X.-F. Zhou, X. Zhang, Q. Zhu, H. Dong, M. Zhao, and A. R. Oganov, *Nano Lett.* **15**, 6182 (2015).
- [72] J. Li and R. Hoffmann, *Chem. Mater.* **1**, 83 (1989).
- [73] T. A. Albright, J. K. Burdett, and M. H. Whangbo, *Orbital Interactions in Chemistry* (Wiley & Sons, New York, 2013).